


Angle-of-arrival detection of radio-frequency waves via Rydberg-atom fluorescence imaging of standing waves in a glass vapor cell

Noah Schlossberger^{1,*}, Rajavardhan Talashila^{1,2}, Nikunj Kumar Prajapati¹, and Christopher L. Holloway¹

¹*National Institute of Standards and Technology, Boulder, Colorado 80305, USA*

²*Department of Electrical Engineering, University of Colorado, Boulder, Colorado 80309, USA*

 (Received 28 April 2025; revised 26 June 2025; accepted 22 July 2025; published 22 August 2025)

We present a method for measuring the angle of arrival of 37-GHz radio-frequency (rf) radiation by mapping the standing waves generated in a rectangular glass vapor cell. These standing waves have regular and well-defined structure from which we can infer the angle and sign of the wavevector of the rf field. We map the field using spatially resolved light sheet spectroscopy of Rydberg states of rubidium atoms in the cell. Unlike traditional phased arrays, this detection scheme is compact, has an active area of nearly 4π steradians, and is sensitive to all rf polarizations. For in-plane measurements ($\phi = 0$), we demonstrate quantitative angle-of-arrival measurements with an uncertainty of the order of 1° in an 11-s measurement, and for out-of-plane measurements (arbitrary θ, ϕ), we demonstrate angle-of-arrival detection with uncertainty of the order of several degrees.

DOI: [10.1103/6dl6-754w](https://doi.org/10.1103/6dl6-754w)

I. INTRODUCTION

Angle-of-arrival measurements of radio-frequency (rf) radiation have many applications in industry and defense [1], including wireless communication [2], radar tracking [3], electronic warfare [4], and navigation systems [5]. Classically, angle of arrival is determined using phased-array antennas [6], which consist of spatially separated receivers that detect the relative phase at each point. While phased arrays are effective, they have several drawbacks: they are technologically complex, they scatter and absorb the incoming radiation, their active area is often limited to one hemisphere, and they tend to have a large radar cross section. We develop a detection scheme that solves these issues by imaging the rf standing waves formed between the walls of a rectangular glass cell of atomic vapor.

Rydberg states of alkali atoms in atomic vapor have been demonstrated as effective traceable sensors of electromagnetic radiation with minimal perturbation to the fields they intend to measure [7,8]. These sensors measure the electric field's perturbation to these states spectroscopically using electromagnetically induced transparency

(EIT). A resonant rf field will induce a splitting in the energy of the Rydberg state proportional to the amplitude of the electric field. With a local oscillator, the phase of the incoming radiation can be measured [9], which allows for angle-of-arrival detection in Rydberg sensors [10–16], but at the cost of the local oscillator emitting radiation (some recent techniques can resolve phase without a local oscillator, but these require extra lasers and a k -vector-aligned rf field [17,18]). To avoid this, an all-optical technique was demonstrated [19] for measuring angle of arrival by generating a standing wave using a metal plate inside of a vapor cell and taking a two-point measurement of the resulting standing wave. Limitations of this technique arise due to limited active angle and difficulty in determining the sign of the angle of arrival.

Recently, we developed a spatially resolved detection method using fluorescence imaging that allows the EIT spectrum to be measured simultaneously at every point in a plane, thus allowing us to “image” the rf field inside a vapor cell [20]. After using this technique to study surface effects [21], we now turn it to angle-of-arrival measurements. It has been demonstrated that the dielectric walls of atomic vapor cells cause reflections and standing waves of the rf incident fields inside the vapor cells [22,23]. Here we use a rectangular vapor cell with thick walls of the order of $1/4$ of the rf wavelength in order to generate strong standing-wave patterns, which have well-defined structure that is dependent on the angle of incidence. We then image these standing waves using fluorescent detection, and fit the profiles to determine the angle of arrival. In

* Contact author: noah.schlossberger@nist.gov

Published by the American Physical Society under the terms of the [Creative Commons Attribution 4.0 International](https://creativecommons.org/licenses/by/4.0/) license. Further distribution of this work must maintain attribution to the author(s) and the published article's title, journal citation, and DOI.

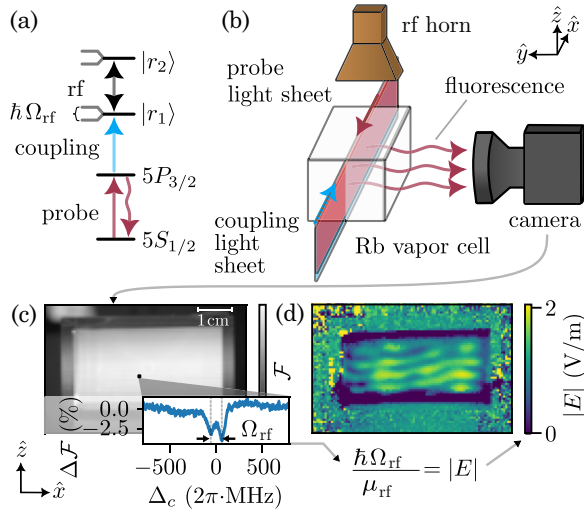


FIG. 1. Scheme for measuring the electric field in a plane using Rydberg atoms. (a) Energy-level diagram of the spectroscopic readout. (b) Layout of the detection scheme. (c) The fluorescence \mathcal{F} is recorded on the image as the detuning of Δ_c as the coupling laser is scanned. The profile of the change in fluorescence $\Delta\mathcal{F}$ as a function of the laser frequency is fitted at each pixel to find the induced splitting Ω_{rf} . (d) The result is a spatial profile of $|E|$ using Eq. (1).

this scheme, the interaction of the radiation with the vapor cell walls, which limits the accuracy of previous phase-based angle-of-arrival measurements [24], is actually the interaction that gives angle-of-arrival resolution.

II. DETECTION SCHEME

Our detection scheme uses the same principle as that of Ref. [20]. We probe the Rydberg state via two-photon EIT in ^{85}Rb [Fig. 1(a)]. Here, $|r_1\rangle$ and $|r_2\rangle$ are two Rydberg states, with which the rf is resonant. We read out the transparency via the decrease in fluorescence of the intermediate $5P_{3/2}$ state, which we image with a camera in the y axis to give spatial resolution in x and z [Fig. 1(b)]. Due to the Autler-Townes effect, the rf field induces an energy splitting in $|r_1\rangle$ given by

$$\hbar\Omega_{\text{rf}} = \mu_{\text{rf}}|E|, \quad (1)$$

where \hbar is Planck's constant, Ω_{rf} is the Rabi frequency of the rf field, μ_{rf} is the transition dipole moment between states $|r_1\rangle$ and $|r_2\rangle$, and $|E|$ is the amplitude of the rf field applied. We read out this energy splitting spectroscopically by scanning the frequency of the coupling laser [Fig. 1(c)]. Fitting the spectrum measured at each pixel to find the Rabi frequency Ω_{rf} , and thus the field magnitude via Eq. (1), we get a spatially resolved image of the magnitude of the rf field [Fig. 1(d)]. One field distribution measurement takes approximately 11 s, limited by the integration time required for adequate signal-to-noise ratio.

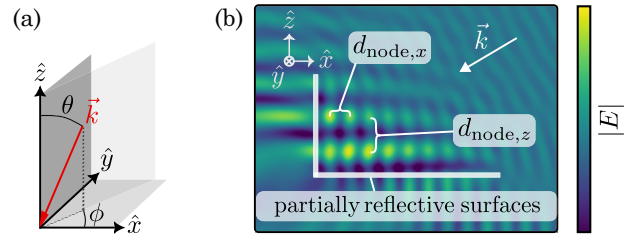


FIG. 2. Principle of the angle-of-arrival scheme. (a) Definition of the coordinate system used in this paper. (b) Modeled standing-wave pattern of light incident on two orthogonal partially reflective surfaces. The field is presented in the x - z plane with a k -vector at $\theta = 60^\circ$, $\phi = 0$.

III. PLANAR MEASUREMENTS ($\phi = 0$)

Consider the case of wavevectors constrained to the x - z plane, or in spherical coordinates, $\phi = 0$ [Fig. 2(a)]. In the presence of two partially reflective surfaces in the z - y and x - y planes, the reflected fields interfere with each other, creating the field distribution shown in Fig. 2(b).

The result is a standing wave whose amplitude is a regular grid of points with a well-defined spacing that is dependent on θ . This can be approximated by summing the incident and reflected waves, and integrating over time to find the the root mean square (RMS) amplitude of the field. Doing this yields

$$\begin{aligned} E_{\text{RMS}} &= E_0 + E_1 |\cos(k_x x) \cos(k_z z)| \\ &= E_0 + E_1 \left| \cos\left(x \frac{2\pi}{\lambda} \sin\theta\right) \cos\left(z \frac{2\pi}{\lambda} \cos\theta\right) \right|, \end{aligned} \quad (2)$$

where \vec{k} is the wavevector and λ is the wavelength of the rf field. Here, E_0 is a constant field amplitude due to the non-interfering portion of the field and E_1 is the amplitude of the standing waves. From this we can get the node spacing:

$$\begin{cases} d_{\text{node},x} = \frac{\lambda}{2 \sin\theta}, \\ d_{\text{node},z} = \frac{\lambda}{2 \cos\theta}. \end{cases} \quad (4)$$

Note that we get purely vertical fringes at $\theta = 0$ and only horizontal fringes at $\theta = \pi/2$.

In a rectangular vapor cell, the glass walls of the vapor cell are partially reflective to rf radiation, representing the set of partially reflective surfaces described above. The other two walls of the vapor cell also cause reflections, but this mostly acts to attenuate the field inside the cell and introduces phase distortions due to its finite thickness. The simple model still qualitatively predicts the standing waves observed inside the vapor cell and encapsulates the relevant degrees of freedom.

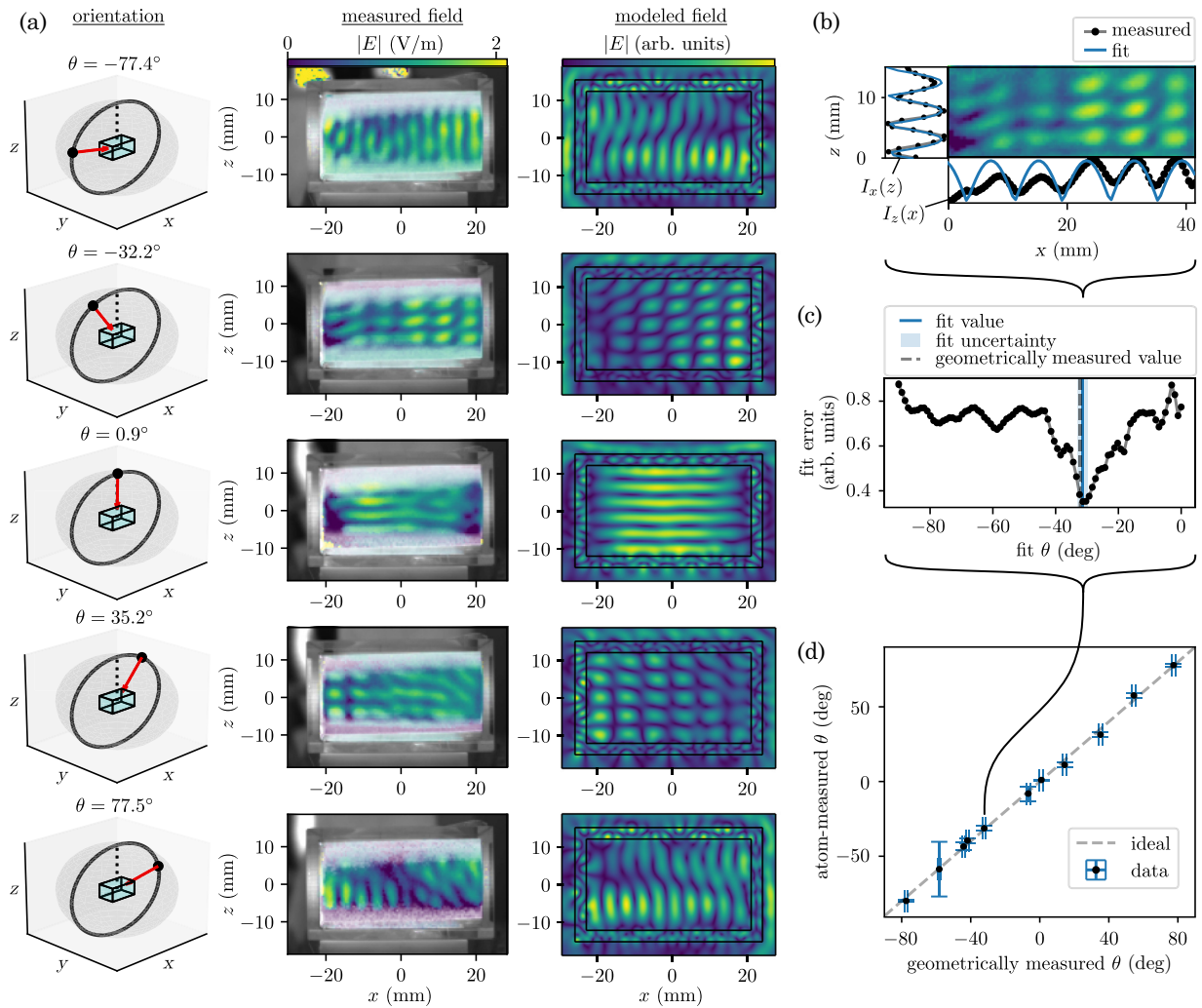


FIG. 3. Standing waves of 36.8951-GHz radiation measured via the $|r_1\rangle = 39D_{5/2} \rightarrow |r_2\rangle = 40P_{3/2}$ level scheme at various values of θ . (a) Left: the geometrically measured angle to the horn antenna. Middle: grayscale images of the vapor cell, with the measured field overlaid in color. The field is masked by the signal-to-noise ratio of the EIT spectrum such that the field is only shown where it is accurately measured. Right: finite-element simulation of the vapor cell in two dimensions assuming an incident plane wave. (b) At $\theta = -32.2^\circ$, the fluorescence image of the field is integrated in x and z , and fitted to Eq. (4) to find θ . (c) The fit error defined in Eq. (5) is plotted for this field distribution. (d) The fit is performed over a series of field distributions measured at different angles and the fitted atom-measured θ is compared with the geometrically measured θ from the vapor cell to the rf horn.

The standing waves are measured at $\phi = 0$ for a variety of θ as shown in Fig. 3(a). We compare the measured field distributions with a finite-element simulation using the measured cell geometry. To make the simulation computationally tractable, we simulate in two dimensions (assuming the vapor cell is infinitely long in y). We get qualitative agreement between the measured and simulated fields. One feature of note is that the fields have complicated structure near the entry point, and have stronger and more regular standing-wave patterns on the other side of the cell. This is most likely due to warping of the phase front as the wave enters the cell due to refraction through the glass. By the time the wave reaches the other end of the cell, these near-field effects are minimized since the wave

has traveled several wavelengths, and the reflections off the far side do not exhibit this effect since they have not passed through any glass. While these distortions near the entry point may reduce fitting robustness, they can differentiate the entrance and exit ports, i.e., the *sign* of the k -vector.

To quantitatively determine the angle of arrival, we crop the image to the region where the fields are well resolved and integrate the measured field distributions along x to produce a one-dimensional profile $I_x(z)$ and along z to produce a one-dimensional profile $I_z(x)$ [Fig. 3(b)]. These profiles will then exhibit the periodicity given by Eq. (4), and the integration will average away the complicated near-field structure at the location of incidence. As we know λ and have calibrated the pixel size using the width

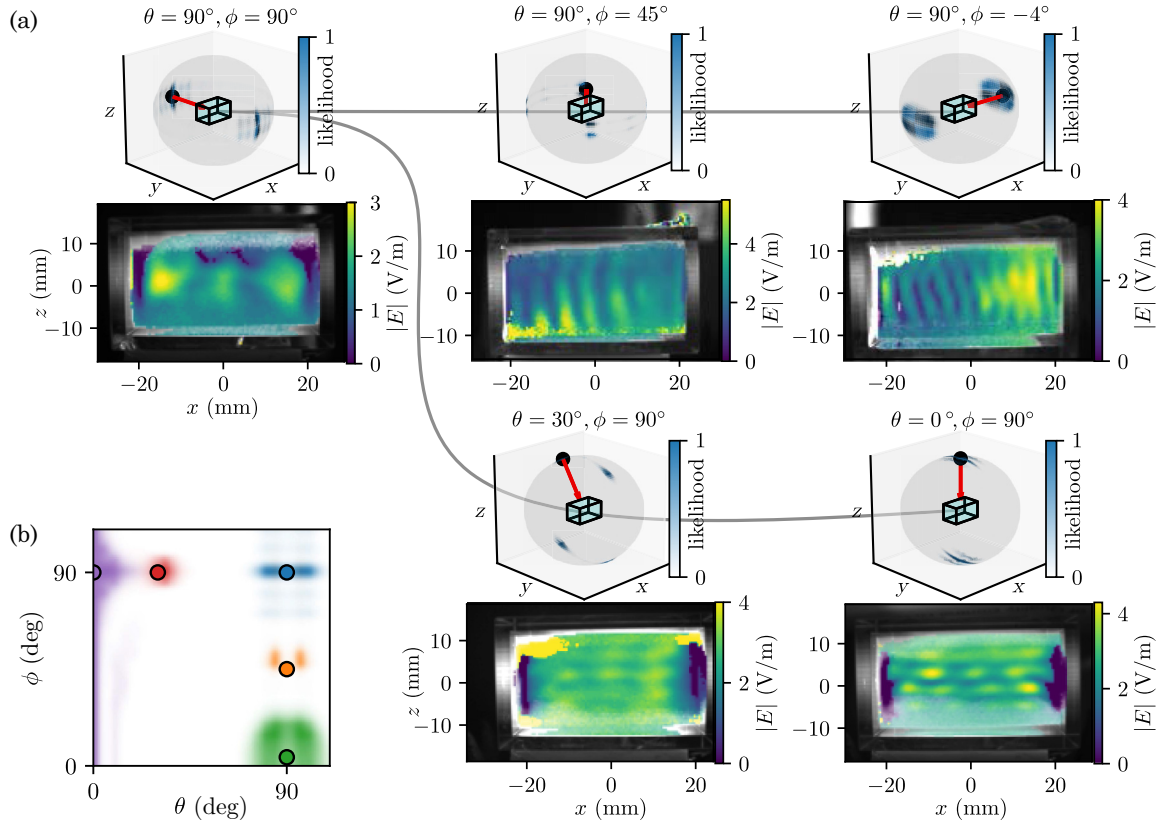


FIG. 4. Standing waves of 37.0727-GHz radiation measured via the $|r_1\rangle = 40D_{5/2} \rightarrow |r_2\rangle = 39F_{7/2}$ level scheme at various values of θ and ϕ . (a) The field distributions are given for each angle. Above each field distribution, the geometrically measured angle of arrival is indicated with a red arrow. We then calculate the likelihood estimator given by Eq. (8) and shade the unit sphere to indicate the estimated three-dimensional angle of arrival. Unlike in the planar measurements, it is not clear that we can discern the sign of the angle of arrival, so all quadrants are shaded. (b) All measurements are overlaid, with circles representing the set angles and the shading representing the resulting likelihood estimator.

of the vapor cell, we can then perform a combined fit of these two profiles to recover θ . We minimize the residual of a sinusoid-magnitude floating θ and an initial phase for each dimension $\phi_{0,x}$ and $\phi_{0,z}$. We define the fit error as

$$\text{fit error}(\theta) \equiv \min_{\phi_{0,x}} \left(\min_{\phi_{0,z}} \left(\frac{1}{L_x} \int_0^{L_x} \left| \cos \left(\frac{2\pi \sin \theta}{\lambda} x + \phi_{0,x} \right) \right| - I_x(x) \right) dx + \frac{1}{L_z} \int_0^{L_z} \left| \cos \left(\frac{2\pi \cos \theta}{\lambda} z + \phi_{0,z} \right) \right| - I_z(z) \right) dz \right), \quad (5)$$

where L_x and L_z are the lengths of the region of measured field in x and z , respectively. The fitted θ is found by minimizing this function, and the uncertainty of the fit is taken to be the width at which the minimum in fit error increases by 5% of the overall dip height [Fig. 3(c)]. In Fig. 3(d), we perform this fit over a range of angles limited by our optical setup. We find agreement between the geometrically

measured angle between the vapor cell and the horn and the fitted angle of arrival, with about 1° of uncertainty in the θ measured with the standing waves.

IV. THREE-DIMENSIONAL EXTENSION

Let us now consider a general k -vector in three dimensions, allowing a nonzero ϕ . The equivalent node spacing as in Eq. (4) becomes

$$\begin{cases} d_{\text{node},x} = \frac{\lambda}{2 \sin \theta \cos \phi}, \\ d_{\text{node},y} = \frac{\lambda}{2 \sin \theta \sin \phi}, \\ d_{\text{node},z} = \frac{\lambda}{2 \cos \theta}. \end{cases} \quad (6)$$

Since we are measuring in the x - z plane, we do not have access to $d_{\text{node},y}$, but $d_{\text{node},x}$ and $d_{\text{node},z}$ contain enough degrees of freedom to constrain θ and ϕ .

For a field incident from an arbitrary direction, the polarization of the radiation is most likely not aligned in a particular axis. The $D_{5/2} \rightarrow P_{3/2}$ transition used in the previous section is sensitive to the polarization, as the relative

polarizations between the optical and rf photons can lead to population in $m_F = 5/2$, which does not have any dipole-allowed transitions for π -polarized microwaves and is thus insensitive to rf radiation. This leads to a central peak in the EIT spectra. While this can be used to extract information about the polarization [19], it significantly reduces the signal-to-noise ratio of the split portion of the population for certain polarizations. To make a robust angle-of-arrival detector for an arbitrary polarization, we now move to a $D_{5/2} \rightarrow F_{7/2}$ transition for sensing so that there will be no rf-insensitive population. In this scheme, the polarization can affect the strength of the splitting (due to the different transition dipole moments between m_F states), but this acts as an overall scaling factor of the standing-wave profile, which still allows accurate angle-of-arrival estimation.

We perform the measurement at a variety of θ and ϕ values in Fig. 4, demonstrating the $\cos\theta$ dependence in tilting axis and the $\cos\phi$ dependence in the other axis. For each angle, we once again integrate both dimensions and perform a simultaneous fit to find the angle of incidence. Now, the objective function is given by

$$\text{fit error}(\theta, \phi) \equiv \min_{\phi_{0,x}} \left(\min_{\phi_{0,z}} \left(\frac{1}{L_x} \int_0^{L_x} \left| \cos \left(\frac{2\pi \sin\theta \cos\phi}{\lambda} x + \phi_{0,x} \right) - I_x(x) \right| dx + \frac{1}{L_z} \int_0^{L_z} \left| \cos \left(\frac{2\pi \cos\theta}{\lambda} z + \phi_{0,z} \right) - I_x(z) \right| dz \right) \right). \quad (7)$$

We then define a “likelihood” estimator as

$$\text{likelihood}(\theta, \phi) = \left(\frac{\max(\text{fit error}) - \text{fit error}(\theta, \phi)}{\max(\text{fit error}) - \min(\text{fit error})} \right)^N, \quad (8)$$

where N is empirically chosen to have value 12 in order to give contrast.

With this, we are able to discern $|k_x|$, $|k_y|$, and $|k_z|$ with a single planar measurement. We are not able to discern the sign of the k -vectors, so there exists ambiguity as to which octant the wave is incident from. The angular uncertainty in the three-dimensional case varies for different angles of incidence, but is generally of the order of several degrees for both θ and ϕ . Note that ϕ is not well defined at $\theta = 0$, which is why our algorithm cannot determine ϕ in this case in Fig. 4(b). The uncertainties are generally greater compared with the planar case because the same spatial structure is used to fit two degrees of freedom instead of one, and the patterns are less ideal due to near-field scattering structure from the windows along the y axis. In this configuration, we are subject to some error due to misalignment between the light sheets and the x - z plane of the vapor cell, as this can cause the spatial distribution to reflect the

z -axis nodes. We believe this is responsible for the field “hot spots” that appear in our $\theta = 90^\circ$ measurements.

V. CONCLUSION

We have demonstrated angle-of-arrival detection of 37-GHz radiation by measuring the periodicity of the standing-wave pattern in a rectangular vapor cell. In a plane, we quantitatively determine the angle with approximately 1° of uncertainty in an 11-s measurement. We measure over the range of our swingarm, from -80° to 80° , but the technique has a capability to detect over a full 360° . In addition, we demonstrate that for most angles we can determine the sign of the k -vector in addition to the angle. We generalize this to three-dimensional angle-of-arrival detection, showing that the standing waves are sensitive to both θ and ϕ .

In this demonstration, we have measured fields of order V/m. For this detection scheme, the field needs to be strong enough to alter the spectrum to a measurable extent, meaning that the rf Rabi rate must be of the order of some fraction of an EIT linewidth, on the scale of MHz. However, a weak microwave field could be detected in the amplitude regime [25]. This would require measuring the background EIT amplitudes with the rf field off in order to compensate for spatial gradients in EIT height due to the laser intensity profiles.

In the future, developing a fiber-coupled version of this probe would improve the accuracy of the angle-of-arrival detector by reducing the scattering of the rf field induced by nearby optics, and would allow one to realize a true 4π -steradian active solid angle, which is currently limited by our optical table.

VI. METHODS

Both beams were expanded into light sheets using prism pairs and cylindrical lens pairs. They were overexpanded and clipped to 25 mm in order to produce a flat-top beam profile along z . Both beams had a Gaussian profile in y , with a full width at half maximum of 1.00 mm. Both light sheets were polarized along the y axis. The coupling and probe laser powers were 209 and 2.9 mW, respectively. The fluorescence was imaged through a 715-nm colored glass longpass filter by a complementary metal oxide semiconductor (CCD) camera with a commercial compound lens placed 9 cm away from the plane of excitation. The probe laser was locked to a reference vapor cell using saturated absorption spectroscopy. The coupling laser was scanned over a range of $2\pi \times 244$ MHz in 11 s while the camera recorded at a frame rate of 20 frames per second (an integration time of 50 ms per frame). The rf horn was mounted on a rotatable swingarm with its center axis coincident with the center of the cell. The measured θ was found in software from a webcam image of the swingarm taken normal to the plane of rotation. A reference edge was placed

parallel to the wall of the cell to define \hat{z} , and the angle of the swingarm was referenced to this surface. The uncertainty in this measured angle of arrival was around 1° , arising from geometric optics and image projection effects. The distance from the horn to the cell was 80 cm, with a horn aperture of $10 \text{ mm} \times 7 \text{ mm}$, justifying the treatment of the incident field as a plane wave. The vapor cell, which was at room temperature and not temperature-stabilized, had outer dimensions of 30 mm in x , 30 mm in y , and 49.5 mm in z . The walls, which were 3 mm thick, were made from PYREX® glass [26], which has a relative permittivity of 4.6 at 1 MHz [27]. We used this value in the finite-element model in Fig. 3, assuming (for lack of sufficient data) that the dielectric constant is similar near 40 GHz. The thickness of the cell walls was chosen to be of the order of a quarter of the wavelength in the material to maximize reflections, though the exact thickness was not important as significant standing waves would be generated as long as the thickness of the cell was not negligible compared with the rf wavelength. The vapor cells had no visible Rb condensation (which could cause rf scattering), and adsorbed Rb on the walls of the cell was not an issue as we were only interested in the spatial distribution of the standing waves rather than their amplitude.

ACKNOWLEDGMENTS

This research was supported by NIST under the NIST-on-a-Chip program. A contribution of the U.S. government, this work is not subject to copyright in the United States.

The authors declare no conflict of interest.

DATA AVAILABILITY

The data that support the findings of this article are openly available [28].

- [1] P. K. Eranti and B. D. Barkana, An overview of direction-of-arrival estimation methods using adaptive directional time-frequency distributions, *Electronics* **11**, 1321 (2022).
- [2] M. I. Nabeel, K. Singh, M. U. Afzal, D. N. Thalakituna, and K. P. Esselle, Dual-band passive beam steering antenna technologies for satellite communication and modern wireless systems: A review, *Sensors* **24**, 6144 (2024).
- [3] M. I. Skolnik, *Radar Handbook* (McGraw-Hill, New York, 2008), 3rd ed., Comprehensive reference on radar systems and technologies.
- [4] A. Spezio, Electronic warfare systems, *IEEE Trans. Microw. Theory Tech.* **50**, 633 (2002).
- [5] J. E. Evans, D. F. Sun, and J. R. Johnson, Of advanced signal processing techniques to angle of arrival estimation in ATC navigation and surveillance systems, Tech. Rep. TR-582, FAA-RD-82-42 (Massachusetts Institute of Technology, Department of Civil Engineering, Cambridge, MA, United States, 1982), pagination: 383 p., <https://www.ntis.gov/>.
- [6] Z. Chen, G. Gokeda, and Y. Yu, *Introduction to Direction-Of-Arrival Estimation* (Artech House, Norwood, MA, 2010).
- [7] N. Schlossberger, N. Prajapati, S. Berweiger, A. P. Rotunno, A. B. Artusio-Glimpse, M. T. Simons, A. A. Sheikh, E. B. Norrgard, S. P. Eckel, and C. L. Holloway, Rydberg states of alkali atoms in atomic vapour as SI-traceable field probes and communications receivers, *Nat. Rev. Phys.* **6**, 606 (2024).
- [8] J. A. Sedlacek, A. Schwettmann, H. Kübler, R. Löw, T. Pfau, and J. P. Shaffer, Microwave electrometry with Rydberg atoms in a vapour cell using bright atomic resonances, *Nat. Phys.* **8**, 819 (2012).
- [9] M. T. Simons, A. H. Haddab, J. A. Gordon, and C. L. Holloway, A Rydberg atom-based mixer: Measuring the phase of a radio frequency wave, *Appl. Phys. Lett.* **114**, 114101 (2019).
- [10] A. K. Robinson, N. Prajapati, D. Senic, M. T. Simons, and C. L. Holloway, Determining the angle-of-arrival of a radio-frequency source with a Rydberg atom-based sensor, *Appl. Phys. Lett.* **118**, 114001 (2021).
- [11] A. Gill, A. Buikema, S. Sirisky, and H. Clevenson, Microwave phase mapping and angle-of-arrival detection using Rydberg atom-based electrometry, *ArXiv:2503.22864*.
- [12] R. Mao, Y. Lin, Y. Fu, Y. Ma, and K. Yang, Digital beamforming and receiving array research based on Rydberg field probes, *IEEE Trans. Antennas Propag.* **72**, 2025 (2024).
- [13] T. Gong, C. Yuen, C. M. S. See, M. Debbah, and L. Hanzo, Rydberg atomic quantum receivers for multi-target DOA estimation, *ArXiv:2501.02820*.
- [14] L. Scorrano, S. Maddio, G. Pelosi, and S. Selleri, in *2021 XXXIVth General Assembly and Scientific Symposium of the International Union of Radio Science (URSI GASS)* (Institute of Electrical and Electronics Engineers, Piscataway, NJ, 2021), p. 1–4.
- [15] Y. Yan, J. Yuan, L. Zhang, L. Xiao, S. Jia, and L. Wang, Three-dimensional location system based on an l-shaped array of Rydberg atomic receivers, *Opt. Lett.* **48**, 3945 (2023).
- [16] P. K. Elgee, K. C. Cox, J. C. Hill, P. D. Kunz, and D. H. Meyer, Electrically small Rydberg sensor for three-dimensional determination of radio-frequency k -vectors, *Phys. Rev. Appl.* **23**, 064022 (2025).
- [17] S. Borówka, M. Mazelanik, W. Wasilewski, and M. Parniak, Optically-biased Rydberg microwave receiver enabled by hybrid nonlinear interferometry, *ArXiv:2403.05310*.
- [18] M. Schmidt, S. M. Bohachuk, V. Venu, R. Wang, H. Kübler, and J. P. Shaffer, All-optical radio-frequency phase detection for Rydberg atom sensors using oscillatory dynamics, *ArXiv:2505.00595*.
- [19] R. Talashila, W. J. Watterson, B. L. Moser, J. A. Gordon, A. B. Artusio-Glimpse, N. Prajapati, N. Schlossberger, M. T. Simons, and C. L. Holloway, Determining angle of arrival of radio frequency fields using subwavelength, amplitude-only measurements of standing waves in a Rydberg atom sensor, *ArXiv:2502.09835*.
- [20] N. Schlossberger, T. McDonald, K. Su, R. Talashila, R. Behary, C. L. Patrick, D. Hammerland, E. E. Mikhailov,

- S. Aubin, I. Novikova, C. L. Holloway, and N. Prajapati, Two-dimensional imaging of electromagnetic fields via light sheet fluorescence imaging with Rydberg atoms, [ArXiv:2412.12568](https://arxiv.org/abs/2412.12568).
- [21] L. Patrick, N. Schlossberger, D. F. Hammerland, N. Prajapati, T. McDonald, S. Berweger, R. Talashila, A. B. Artusio-Glimpse, and C. L. Holloway, Imaging of induced surface charge distribution effects in glass vapor cells used for Rydberg atom-based sensors, *AVS Quantum Sci.* **7**, 024401 (2025).
- [22] H. Fan, S. Kumar, J. Sheng, J. P. Shaffer, C. L. Holloway, and J. A. Gordon, Effect of vapor-cell geometry on Rydberg-atom-based measurements of radio-frequency electric fields, *Phys. Rev. Appl.* **4**, 044015 (2015).
- [23] C. L. Holloway, J. A. Gordon, A. Schwarzkopf, D. A. Anderson, S. A. Miller, N. Thaicharoen, and G. Raithel, Sub-wavelength imaging and field mapping via electromagnetically induced transparency and Autler-Townes splitting in Rydberg atoms, *Appl. Phys. Lett.* **104**, 244102 (2014).
- [24] D. Richardson, J. Dee, B. N. Kayim, B. C. Sawyer, R. Wylie, R. T. Lee, and R. S. Westafer, Study of angle of arrival estimation with linear arrays of simulated Rydberg atom receivers, *APL Quantum* **2**, 016123 (2025).
- [25] M. Schmidt, S. Bohaichuk, V. Venu, F. Christaller, C. Liu, F. Ripka, H. Kübler, and J. P. Shaffer, Rydberg-atom-based radio-frequency sensors: Amplitude-regime sensing, *Opt. Express* **32**, 27768 (2024).
- [26] Certain equipment, instruments, software, or materials are identified in this paper in order to specify the experimental procedure adequately. Such identification is not intended to imply recommendation or endorsement of any product or service by NIST, nor is it intended to imply that the materials or equipment identified are necessarily the best available for the purpose.
- [27] Corning Inc., *Corning® PYREX® Glass (SG3.3) Datasheet* (Corning Incorporated, United States, 2023), https://www.corning.com/media/worldwide/csm/documents/PYREX_SG3.3_PI%20Sheet.pdf, accessed: 2025-04-04.
- [28] N. Schlossberger, Data associated with “Angle-of-arrival detection of radio-frequency waves via Rydberg atom fluorescence imaging of standing waves in a glass vapor cell.” (National Institute of Standards and Technology, 2025), <https://doi.org/10.18434/mds2-3801>.